AIAA SciTech Forum
8-12 January 2024, Orlando, FL
AIAA SCITECH 2024 Forum

10.2514/6.2024-1792

Additive Manufacturing and Working Fluid Characterization of Ceramic Heat Pipes

Giancarlo D'Orazio*
Cornell University, Ithaca, NY, 14853, USA

William Sixel †
NASA Glenn Research Center, Cleveland, OH, 44135, USA

Sadaf Sobhani‡
Cornell University, Ithaca, NY, 14853, USA

In this work, additively manufactured (AM) aluminum nitride (AlN) ceramic heat pipes were developed to improve spacecraft heat rejection capabilities beyond the current state-of-the-art metal systems. A low sintering temperature aluminum nitride slurry is developed for digital light processing printing (DLP) and the optimal debinding curves are examined. Printed AlN parts are characterized via SEM and optical profilometry. AlN 3D-printed parts are also tested for compatibility with aluminum bromide, aluminum chloride, and iodine, among other proposed working fluids at 350-600 K in an inert atmosphere, with reactivity measured via SEM and Fourier transform infrared spectroscopy (FTIR).

I. Nomenclature

C	=	constant
D_{cure}	=	depth of cure
d_{part}	=	particle diameter
ε_r	=	rough surface emissivity
ε_s	=	smooth surface emissivity
I	=	light intensity
I_0	=	light intensity to cure resin
n_0	=	resin refractive index
Δ_n	=	difference between refractive index of n_0 and ceramic
ϕ	=	volumetric particle loading
R	=	roughness factor
R_a	=	average surface roughness
R_s	=	contour peak spacing

II. Introduction

Crewed missions to Mars require enormous quantities of energy, both for electrical power and propulsion. In nuclear electric propulsion (NEP) designs, nuclear reactors generate hundreds or thousands of kilowatts of electrical power which can be used for propulsion systems, such as Hall effect thrusters, life support systems, sensors, and a variety of other applications as necessary [1–3]. This massive amount of power comes with a considerable drawback in the form of waste heat. At present, the most effective means of heat rejection relies on pumped fluid loops and heat pipes that would transfer waste heat from the reactor system to radiator panels. These requisite panels are estimated to be hundreds of square meters in combined area, therefore contributing considerably to the total system mass [4, 5]. Heat pipes are common heat rejection components that do not require additional power or moving parts that function through

*Graduate Student, Sibley School of Mechanical and Aerospace Engineering, 184 Grumman Hall, 134 Rhodes Dr., Ithaca, NY 14853
†Aerospace Engineer, Thermal Systems and Transport Processes Branch, Propulsion Division
‡Assistant Professor, Mechanical and Aerospace Engineering, AIAA Member.

Table 1 Comparison of AM and non-AM AlN Compositions

	Composition (wt %)	Sintering Temperature (°C)	Flexural Strength (MPa)	Thermal Conductivity (W/m·K)
Duan et al. 2020 [12]	95:5 AlN:Y_2O_3	1845	265 ± 20	155
Ożóg et al. 2020 [18]	90:6:4 AlN:Y_2O_3:Al_2O_3	1800	Not tested	4.34
Lin et al. 2022 [14]	100:5 AlN:Y_2O_3	1850	365-400	135-150 (appr)
Rauchenecker et al. 2022 [15]	96:3:1 AlN:Y_2O_3:CaO	1700	320-498	162.1-166.2
Lee and Kim 2014 [16] (Basis for this work, non AM)	98:1:1 AlN:Y_2O_3:$CaZrO_3$	1600	579	120

two-phase heat transfer between the evaporator (the heat source) and the condenser (the heat sink). Conventional heat pipes have been flown successfully for decades using traditional manufacturing techniques, such as metal sintering, cold rolling, extruding, and forming [6]. More recently, metal additive manufacturing (AM) has produced greater variety in the internal wick design and reduced some of the manufacturing challenges associated with bonding a wick to the envelope material, as these structures can be produced as a monolith in an additive process [7]. These designs meet or exceed the performance of conventional heat pipes, illustrating substantial room for development in this space [8]. For example, AM enables integrated fabrication of the heat pipe and radiator panel in a single part; thereby reducing system complexity and interface efficiency losses.

The design of a heat pipe begins with the identification of its working temperature range, which then allows for the selection of an appropriate working fluid. As a two-phase device, heat pipes can only operate at temperatures between the triple point and critical point of a fluid. However, an even more limited range is usually required because of practical heat load limitations. The envelope material must be carefully matched to the working fluid, as even slow chemical reactions between the envelope and fluid can generate non-condensible gas that causes the heat pipe performance to deteriorate. The operating range for state-of-the-art metal heat pipes, such as ammonia-titanium systems, is 200-400 K [9]. However, the target rejection temperature range associated with the high thermal loads of some NEP systems is 500-600K. This is firmly in the intermediate temperature range for heat pipes and, as a result, is a challenge to select an effective working fluid and envelope combination [10]. One approach to achieve higher operating temperatures is to apply ceramic heat pipes as this could enable many new working fluids that were previously incompatible with metal envelopes. A ceramic of particular interest for this application is aluminum nitride (AlN), owing to its high thermal conductivity of up to 320 W/m·K, high dielectric strength, moderate to high flexural strength, and low chemical reactivity [11]. As a material, AlN has been investigated for use in AM systems using digital light processing (DLP) wherein ceramic particles are mixed with a photosensitive resin, and parts are built up in a layerwise fashion via exposure to near-UV light. DLP enables the use of small particle sizes in the sub-micron range and provides a better final density of the printed part and, therefore, enhanced mechanical and thermal properties compared to other processes, such as binder jetting.

Investigations of AlN AM processes have primarily considered conventional AlN formulations utilizing on yttria and alumina as liquid state sintering aids [12–14]. While these formulations are well characterized, sintering temperatures typically exceed 1800°C, which significantly limits processing to select furnaces due to the high temperature requirements. Calcium oxide has been considered as an additive, which lowers the sintering temperature to 1700°C, while maintaining good flexural strength and thermal conductivity [15]. This work considers a lower temperature formulation not previously used in an additive process leveraging yttria and calcium zirconate with sintering temperatures as low as 1600°C with high flexural strength and thermal conductivity [16]. A summary of the various AM compositions has been summarized in Table 1, including sintering temperature, flexural strength, and thermal conductivity [17].

In this work, AlN ceramic heat pipes are 3D printed to leverage the material advantages of ceramics and the geometric advantages of the AM process. The compatibility of 3D-printed AlN with several working fluids relevant to NEP intermediate-temperature systems is experimentally tested, including aluminum bromide ($AlBr_3$), aluminum chloride ($AlCl_3$), iron chloride ($FeCl_3$), iodine (I_2), and Dowtherm A. While these working fluids have been trialed with conventional envelope materials [19], the enhanced compatibility provided by a ceramic material coupled to the ability

to operate in both intermediate and high temperature regimes provides an unique pathway forward for heat pipe design.

III. Materials and Methods

Initial ceramic slurries used in the 3D printer were developed using 500 nm aluminum nitride and 10 nm yttria powders (US NanoMaterials) in a 100:5 AlN to Y_2O_3 weight ratio, which enables liquid-state sintering and produces a high density ceramic. This formulation requires both high sintering temperature for full densification (1850°C) while the AlN particle diameter produces a low depth of cure. Subsequent work utilized AlN powder with a larger average particle diameter, specifically, 0.8-2.0 μm Höganäs Grade C AlN to increase the depth of cure for the base slurry. Powders are heated to 150°C for 12 hours to remove any ambient moisture, then mixed with 1% weight with a dispersant (Hypermer KD1) in an acetone carrier at 800 RPM in a Speedmixer Flacktek mixer to prevent flocculation of the ceramic particles. The acetone is then evaporated at 35 °C, the dry powders are sieved in stages down to 53 μm then undergo vacuum desiccation for 12 hours. The powders are then mixed at 40%/volume with a photosensitive resin (Admatec, Development Resin C) under vacuum in a mixer in stages from 800 to 1200 RPM. The viscosity of the resultant ceramic-resin slurry was tested using rheometry (TA Instruments DHR3 Rheometer) to ensure compatibility with the 3D printer.

Depth of cure tests are first conducted to determine the optimal print layer height and light dosage on an Admatec Admaflex 130 DLP printer. Since particle size is inversely proportional to required dose, larger particle size AlN will be used to increase depth of cure at the same light intensity, per Equation 1, related to the Beer-Lambert law:

$$D_{cure} \approx \frac{C}{\phi} \cdot d_{part} \left(\frac{n_0}{\Delta_n}\right)^2 \cdot ln\left(\frac{I}{I_0}\right) \tag{1}$$

Where D_{cure} is the depth of cure, C is a constant such as light wavelength, ϕ is the volumetric particle loading, d_{part} is the ceramic particle diameter, n_0 is the refractive index of the base resin, Δ_n is the difference between the refractive index of n_0 and the ceramic particles, I is light intensity to cure the loaded resin, and I_0 is the light intensity required to cure unloaded resin.

Thermogravimetric analysis (TA Instruments 5500) was performed at a rate of 2°C/min to 1000°C on the cured ceramic-resin slurry to develop an optimal debinding curve, wherein the photosensitive resin is burned off from the ceramic, yielding a green body which contains only trace levels of organic contaminants. After debinding, parts are sintered to create fully dense ceramics. High sintering temperatures are required for the 100:5/wt% AlN:Y_2O_3 formulation (up to 1850 °C in a nitrogen atmosphere), limiting processing to specialized atmosphere furnaces. A low sintering temperature (1600°C) formulation is therefore investigated using $CaZrO_3$ and Y_2O_3 additives as a means to simplify thermal processing. [20]

The optical properties of the sintered ceramic are of particular interest as they relate to effective emissivity. Most additive manufacturing processes leverage a layerwise production method which leaves characteristic artifacts perpendicular to the print direction where layers are joined. To better characterize the effects of this process, optical profilometry was conducted on sintered specimens both in plane and perpendicular to the print direction. The effect of these artifacts, or layer lines as they are commonly described, can be quantified as having a direct impact on the effective emissivity via a modified Agababov roughness function [21, 22]. An as-printed section of alumina is shown in Figure 1 to illustrate these layer lines. Equations 2 and 3 describe the calculation of the roughness factor, R, and rough surface emissivity, ε_r .

$$R = \left[1 + 4\left(\frac{R_a}{R_s}\right)^2\right]^{-1} \tag{2}$$

Where the roughness factor, R, is a function of the average surface roughness, R_a, and the peak spacing of the contours of interest, R_s, which in this case are the layer lines. With the roughness factor, an estimation of the rough surface emissivity can be calculated using documented emissivity values of a smooth surface, ε_s.

$$\varepsilon_r = \left[1 + \left(\frac{1}{\varepsilon_s} - 1\right) R\right]^{-1} \tag{3}$$

Working fluids explored in this study include aluminum bromide ($AlBr_3$), aluminum chloride ($AlCl_3$), iron chloride ($FeCl_3$), iodine (I_2), and Dowtherm A which is a eutectic composed of diphenyl oxide ($C_{12}H_{10}O$) and biphenyl ($C_{12}H_{10}$).

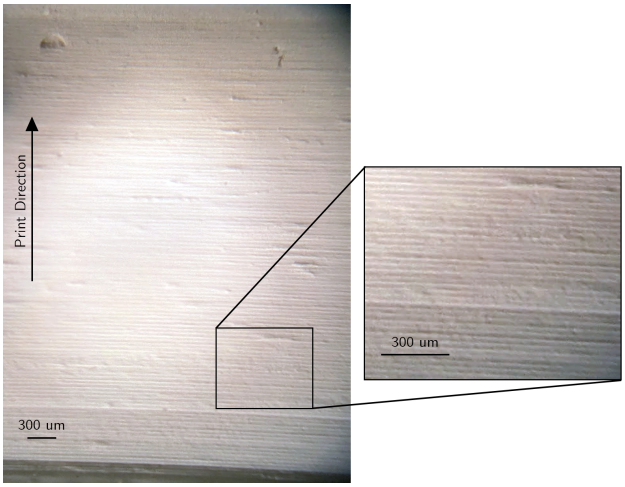

Fig. 1 Alumina test article illustrating layer lines as a result of the printing process, each layer approximately 30 µm in height.

These fluids are suited to the intermediate temperature heat pipe designs in the operating regime of 500-600K [23]. A majority of the working fluids, particularly the halides, are both hygroscopic and reactive to water, and therefore require special handling. As a result, initial testing will be conducted in a controlled dry nitrogen atmosphere to ensure a dry operating environment and prevent hydrolization of the AlN parts.

A 40 watt ceramic-metal heater paired with a temperature controller will provide the correct operating temperature for atmospheric testing, varying between 40 and 315°C depending on the working fluid melting point. AlN samples consisting of rectangular test beam sections will be introduced to the working fluid, contained in a covered quartz crucible, in order to determine reactivity between the fluid and envelope material illustrated in Figure 2. Scanning electron microscope images and Fourier transform infrared spectroscopy (FTIR) was conducted with a Bruker Vertex V80V Vacuum FTIR in order to determine reactivity of the envelope material to the working fluids. Absorption scans were taken from 4000 to 600 cm^{-1} with a resolution of 1 cm^{-1} to determine reactivity of the working fluid to the envelope material.

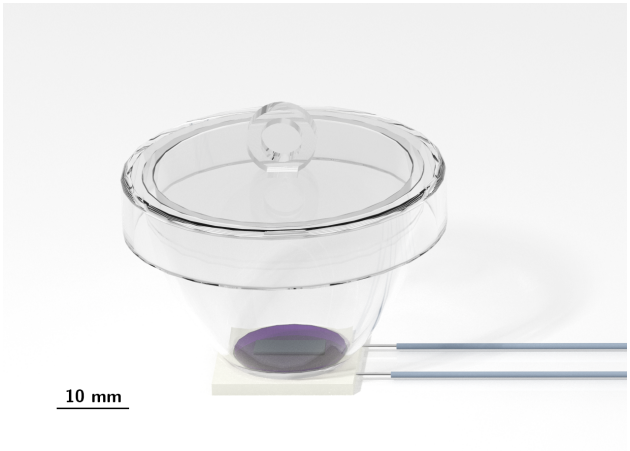

Fig. 2 An image of the basic test setup with quartz crucible mounted to a ceramic heater. Working fluids are heated to liquid state and a beam section immersed.

IV. Results and Discussion

Rheometry testing with 100:5/wt% AlN:Y_2O_3 and 98:1:1/wt% AlN:Y_2O_3:$CaZrO_3$ slurries demonstrated shear thinning behavior, with a representative curve from the AlN:Y_2O_3:$CaZrO_3$ formulation shown in Figure 3. At high shear rates, above 10^1 1/s, the slurry does begin to thicken, however these rates are outside those typically seen in the Admaflex 130 printer as the tape casting speed is user-adjustable, ensuring adequate slurry dispersion.

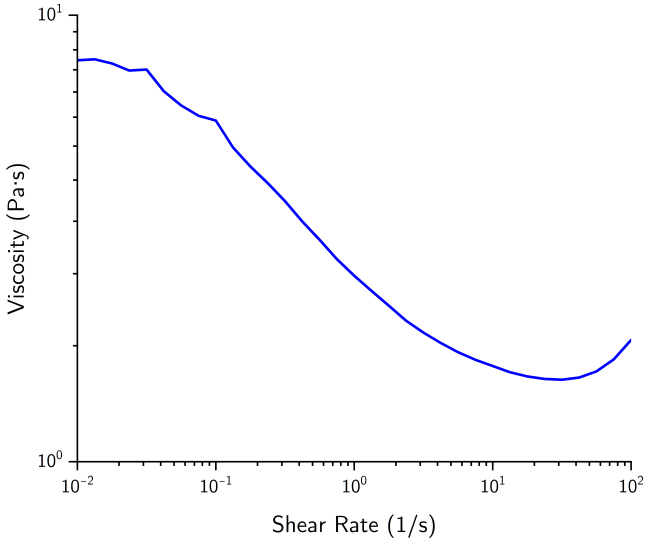

Fig. 3 Frequency sweep results for rheometer testing of the AlN slurry. This shows low viscosity and shear thinning under typical shear rates.

Initial tests with the 500 nm AlN and Y_2O_3 composition were found to produce low cure depth and subsequently limited printing rate due to the small particle size and high refractive index of the powder compared to the base resin. A maximum cure depth of 14 μm with an LED power of 75% and exposure of 30 seconds was found; this is equivalent to approximately 1,035 mJ/cm^2 effective dose per layer. Substituting the Höganäs Grade C AlN powder, with larger mean particle diameter yielded up to 2.5 times greater depth of cure at the same settings, indicating suitability for printing at 20 μm layers. Depth of cure tests with the Höganäs powder paired with Y_2O_3 and $CaZrO_3$ produced a depth of cure of approximately 36 μm with a light dose of 586 mJ/cm^2. At this dose, blurring of sharp edges was evident, producing parts with considerable overexposure and loss of fine feature, as shown in Figure 4B. After testing with various exposure settings, a dose of approximately 414 mJ/cm^2 was found to produce a balance of high resolution parts with an adequate depth of cure of 34 μm.

Thermogravimetric analysis of the as-printed parts showed considerable differences in air and nitrogen atmosphere debinding, with three dominant derivative mass loss peaks for air at approximately 200°C, 345°C, and 450°C compared to a singular peak at approximately 395°C in nitrogen, illustrated in Figure 5. Notably, the air TGA exhibits mass gain beginning at 700°C, owing to oxidation of the sample, increasing its density as AlN was converted to oxynitride and oxide products. In order to prevent oxidation of the AlN, debinding was conducted in nitrogen only.

AlN parts were debound in a packed 50:50/wt% boron nitride and silicon nitride powder bed, to support samples without sintering to the parts during processing. After debinding in nitrogen, the parts were moved to a carbon furnace for final sintering for 3 hours at 1600°C and a subsequent 2 hour hold at 1400°C to facilitate high final part density while minimizing grain coarsening. Figure 6A shows a green body after printing without thermal processing and the final sintered part. In Figure 6B, one can observe detailed gyroid porous structures are preserved throughout thermal processing. The sintered parts were characterized in a Zeiss Gemini 500 SEM to determine pore size and porosity. High levels of porosity were observed in Figure 7, which matches with a shrinkage rate of approximately 11%, however this is lower than the expected 20-30% typical of most ceramics produced with the Admatec printing system. ImageJ analysis of the SEM imagery indicates a surface porosity of approximately 18.6%, with a mean pore size of 301 nm.

Results of optical profilometry of the sintered samples yield in-plane average area surface roughness values (Sa) of

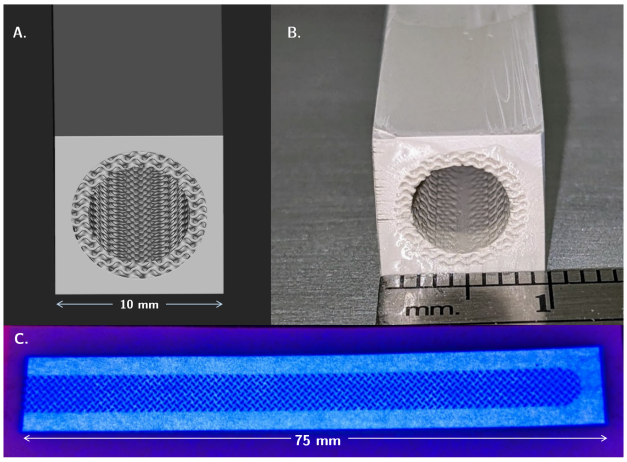

Fig. 4 A. CAD model of a heat pipe section compared B. The as-printed heat pipe before optimization of print settings, with considerable over-curing of the wick section. C. A slice of the heat pipe, as projected by the printer.

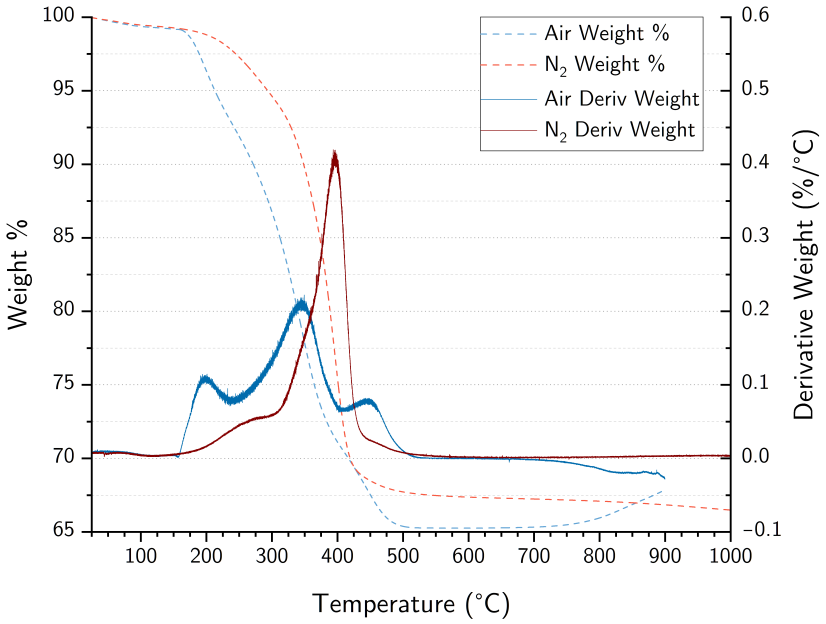

Fig. 5 Thermogravimetric analysis demonstrating the burnout characteristics in air and nitrogen environments.

approximately 1.604 μm compared to 2.589 μm parallel to the print direction, owing to the layer lines created in the printing process. A 3D reconstruction of the sample along layer lines is presented in Figure 7 highlighting the sawtooth pattern created by the printing process at regular intervals correlating to the 20 μm layer height. In both the in-plane and layer line cases, surface roughness may be reduced by polishing, however the effective increase in surface area may be desirable for use in radiators. In the case of the emissivity along layer lines, assuming a smooth surface emissivity of 0.87 yields a roughness factor of 0.937 and an effective emissivity of 0.928. This increase in emissivity is planned to be better characterized experimentally to confirm the theoretical values.

All samples were thoroughly washed with compatible solvents and observed for changes compared to control. AlN samples exposed to the working fluids did not exhibit qualitative mechanical or optical changes, with the exception of iron chloride, which left considerable surface residue on a portion of the material. This residue appeared to be

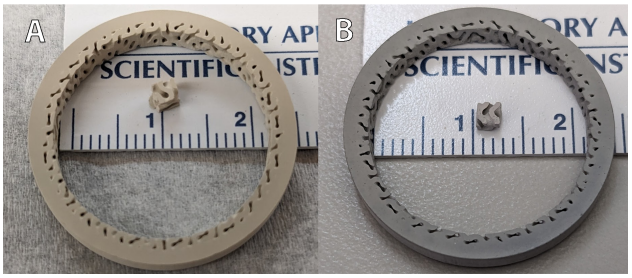

Fig. 6 A. Sample of an as-printed part B. The same part after debinding and sintering

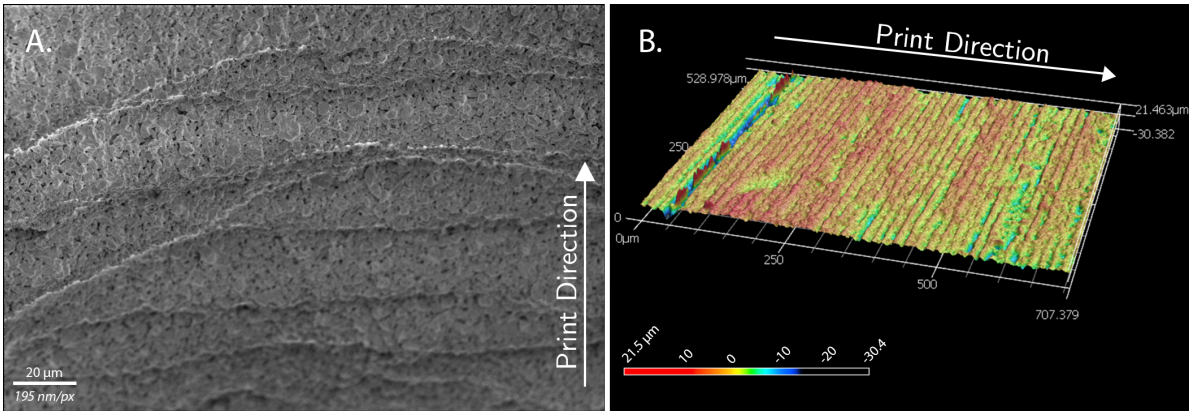

Fig. 7 A. SEM of a gyroid structure, highlighting surface porosity and layer lines from printing. B. 3D reconstruction of a sintered AlN sample based on the results of optical profilometry scans

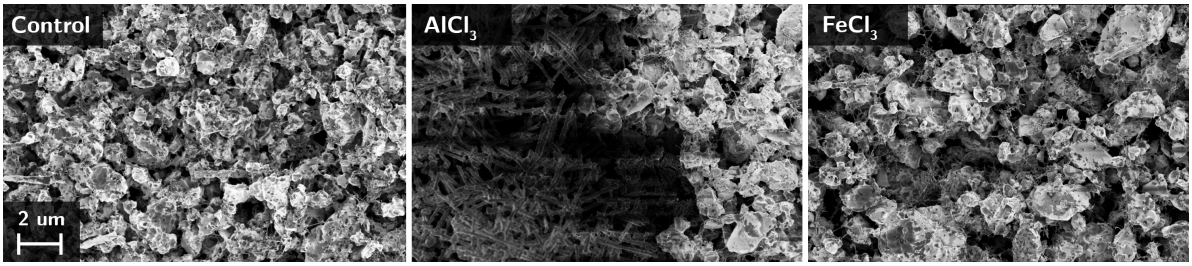

Fig. 8 SEM imagery from the (L to R) control, $AlBr_3$ and $FeCl_3$ working fluid samples. Considerable charging is evident in the regions of the rod-like $AlCl_3$ crystals. The $FeCl_3$ sample exhibits fine web like structures throughout the ceramic pores.

crystallized iron chloride which was not removed by initial solvent washes, however this was removed with subsequent cleanings. SEM analysis of the samples indicated some level of reactivity or interaction with the envelope material in the cases of the $AlCl_3$, $FeCl_3$, and I_2 working fluids, with images of the two chloride compounds shown in Figure 8. These two working fluids resulted in considerable crystal formation in and around pores in the ceramic substrate in spite of numerous solvent washes. Iodine appears to have produced some surface pitting in the exposed sample however this cannot be conclusively correlated strictly to iodine exposure as opposed to defects formed by handling and cleaning. $AlBr_3$ and Dowtherm A did not produce any substantive changes in the surface morphology compared to a control sample.

FTIR analysis demonstrated variation in the samples compared to control, however with the exception of the iodine working fluid sample, alterations to the base ceramic after exposure were minimal, indicating good compatibility with all but the iodine sample as illustrated in Figure 9. Analysis of a variety of iodide compounds indicates a propensity for strong peaks at wavenumbers above 900 cm^{-1}. Additional testing via X-ray photoelectron spectroscopy (XPS) is

planned to better identify the changes in the oxidation state to the envelope material with all working fluids.

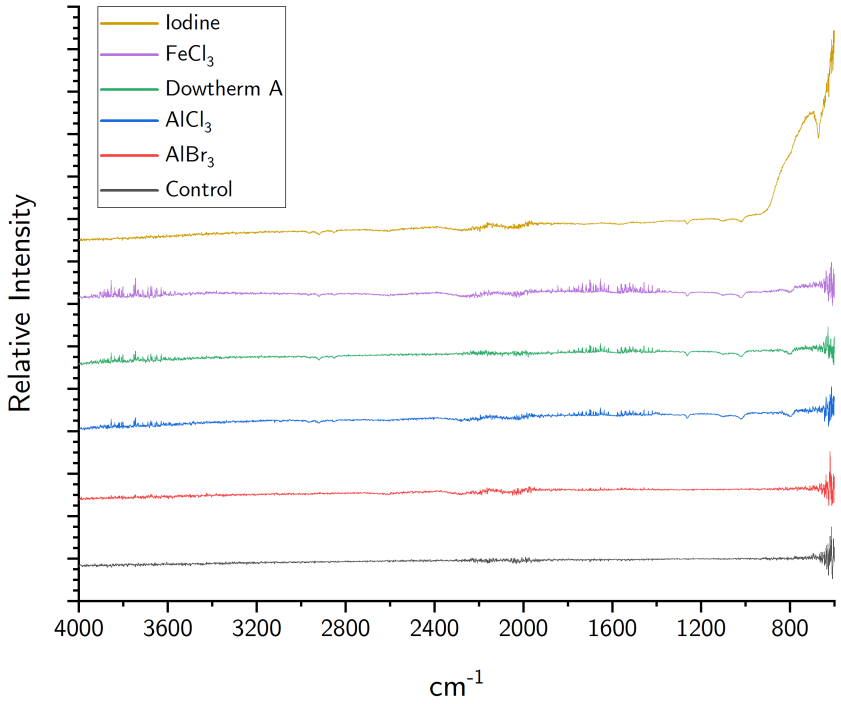

Fig. 9 FTIR analysis of the envelope material after working fluid exposure.

V. Conclusions

In this work, two formulations of aluminum nitride ceramic slurries were trialed. Owing to lower sintering temperature and better depth of cure performance, a formulation consisting of 98:1:1/wt% Höganäs Grade C AlN with calcium zirconate and yttria ceramics was printed, debound and sintered. Thermogravimetric analysis of the as-printed, green ceramics yields debinding curves in both air and nitrogen environments. In air, oxidation of the samples begins as temperatures approach 700 °C therefore a nitrogen debinding curve was utilized in experiments. Densification of the as-printed samples requires additional optimization, as porosity was evident in the sintered parts and shrinkage of the ceramic approached only 10%. The impact of surface texture due to printing artifacts was investigated and determined to increase the effective emissivity along layer lines for the sintered samples.

Working fluid compatibility tests were performed with aluminum bromide, aluminum chloride, ferric chloride, iodine, and Dowtherm A. Surface morphology changes in the envelope material were observed after exposure to the $AlCl_3$, $FeCl_3$, and I_2 working fluids, with crystal formation in the two former cases and surface pitting in the latter. FTIR analysis indicates that compatibility with all tested working fluids was good with the exception of iodine, which had peaks strongly associated with iodide compounds formed during testing. XPS testing is planned to better characterize the oxidation states of the samples and identify changes in chemical composition.

Acknowledgments

This work is funded by NASA Early Stage Innovation grant number 80NSSC23K0236 as part of the Space Technology Research Grants program.

The authors acknowledge the use of facilities and instrumentation supported by NSF through the Cornell University Materials Research Science and Engineering Center DMR-1719875.

The authors acknowledge Lisa Rueschhoff and Connor Wyckoff of the Air Force Research Lab for their support in this project.

References

[1] Pawlik, E. V., and Phillips, W. M., "A Nuclear Electric Propulsion Vehicle for Planetary Exploration," *Journal of Spacecraft and Rockets*, Vol. 14, No. 9, 1977, pp. 518–525. https://doi.org/10.2514/3.57233, URL https://doi.org/10.2514/3.57233, publisher: American Institute of Aeronautics and Astronautics _eprint: https://doi.org/10.2514/3.57233.

[2] Jones, R. M., and Sauer, C. G., "Nuclear electric propulsion missions," *Journal of the British Interplanetary Society*, Vol. 37, 1984, pp. 395–400. URL https://ui.adsabs.harvard.edu/abs/1984JBIS...37..395J, aDS Bibcode: 1984JBIS...37..395J.

[3] Miao, X., Zhang, H., Wang, Q., Xia, Y., and Sun, W., "Optimum design of nuclear electric propulsion spacecraft for deep space exploration," *Energy Reports*, Vol. 8, 2022, pp. 9629–9641. https://doi.org/10.1016/j.egyr.2022.07.146, URL https://www.sciencedirect.com/science/article/pii/S2352484722014123.

[4] Nikitaev, D., Duchek, M. E., Harnack, C., Machemer, W., and Rao, D., "Heat Pipe Heat Exchanger for Nuclear Electric Propulsion Power Conversion System," *ASCEND 2022*, 2022. https://doi.org/10.2514/6.2022-4287, URL https://arc.aiaa.org/doi/abs/10.2514/6.2022-4287, _eprint: https://arc.aiaa.org/doi/pdf/10.2514/6.2022-4287.

[5] Machemer, W. S., Duchek, M. E., and Nikitaev, D., "Considerations for Radiator Design in Multi-Megawatt Nuclear Electric Propulsion Applications," *AIAA SCITECH 2023 Forum*, AIAA SciTech Forum, American Institute of Aeronautics and Astronautics, 2023. https://doi.org/10.2514/6.2023-0152, URL https://arc.aiaa.org/doi/10.2514/6.2023-0152.

[6] Dobran, F., "Heat pipe research and development in the Americas," *Heat Recovery Systems and CHP*, Vol. 9, No. 1, 1989, pp. 67–100. https://doi.org/10.1016/0890-4332(89)90140-3, URL https://www.sciencedirect.com/science/article/pii/0890433289901403.

[7] Robinson, A. J., Colenbrander, J., Deaville, T., Durfee, J., and Kempers, R., "A wicked heat pipe fabricated using metal additive manufacturing," *International Journal of Thermofluids*, Vol. 12, 2021, p. 100117. https://doi.org/10.1016/j.ijft.2021.100117, URL https://www.sciencedirect.com/science/article/pii/S2666202721000550.

[8] MGlen, R. J., "An introduction to additive manufactured heat pipe technology and advanced thermal management products," *Thermal Science and Engineering Progress*, Vol. 25, 2021, p. 100941. https://doi.org/10.1016/j.tsep.2021.100941, URL https://www.sciencedirect.com/science/article/pii/S2451904921001037.

[9] Shukla, K. N., "Heat Pipe for Aerospace Applications—An Overview," *Journal of Electronics Cooling and Thermal Control*, Vol. 05, No. 01, 2015, p. 1. https://doi.org/10.4236/jectc.2015.51001, number: 01 Publisher: Scientific Research Publishing.

[10] Anderson, W. G., Tamanna, S., Tarau, C., Hartenstine, J., and Ellis, D., "Intermediate Temperature Heat Pipe Life Tests and Analyses," *43rd International Conference on Environmental Systems*, American Institute of Aeronautics and Astronautics, Vail, CO, 2013. https://doi.org/10.2514/6.2013-3304, URL https://arc.aiaa.org/doi/10.2514/6.2013-3304.

[11] Baik, Y., and Drew, R. A., "Aluminum Nitride: Processing and Applications," *Advanced Ceramic Materials*, Key Engineering Materials, Vol. 122, Trans Tech Publications Ltd, 1996, pp. 553–0.

[12] Duan, W., Li, S., Wang, G., Dou, R., Wang, L., Zhang, Y., Li, H., and Tan, H., "Thermal conductivities and mechanical properties of AlN ceramics fabricated by three dimensional printing," *Journal of the European Ceramic Society*, Vol. 40, No. 10, 2020, pp. 3535–3540. https://doi.org/10.1016/j.jeurceramsoc.2020.04.004, URL https://www.sciencedirect.com/science/article/pii/S0955221920302594.

[13] Ożóg, P., Rutkowski, P., Kata, D., and Graule, T., "Ultraviolet Lithography-Based Ceramic Manufacturing (UV-LCM) of the Aluminum Nitride (AlN)-Based Photocurable Dispersions," *Materials*, Vol. 13, No. 19, 2020. https://doi.org/10.3390/ma13194219, URL https://www.mdpi.com/1996-1944/13/19/4219.

[14] Lin, L., Wu, H., Ni, P., Chen, Y., Huang, Z., Li, Y., Lin, K., Sheng, P., and Wu, S., "Additive manufacturing of complex-shaped and high-performance aluminum nitride-based components for thermal management," *Additive Manufacturing*, Vol. 52, 2022, p. 102671. https://doi.org/10.1016/j.addma.2022.102671, URL https://www.sciencedirect.com/science/article/pii/S2214860422000768.

[15] Rauchenecker, J., Rabitsch, J., Schwentenwein, M., and Konegger, T., "Additive manufacturing of aluminum nitride ceramics with high thermal conductivity via digital light processing," *Open Ceramics*, Vol. 9, 2022, p. 100215. https://doi.org/10.1016/j.oceram.2021.100215, URL https://www.sciencedirect.com/science/article/pii/S2666539521001619.

[16] Lee, H. M., and Kim, D. K., "High-strength AlN ceramics by low-temperature sintering with CaZrO3–Y2O3 co-additives," *Journal of the European Ceramic Society*, Vol. 34, No. 15, 2014, pp. 3627–3633. https://doi.org/10.1016/j.jeurceramsoc.2014.05.008, URL https://www.sciencedirect.com/science/article/pii/S0955221914002660.

[17] D'Orazio, G. and Sobhani, S., "Additively Manufactured Ceramics for High-Temperature Heat Rejection Systems," *Thermal Fluid Analysis Workshop*, National Aeronautics and Space Administration, College Park, MD, 2023.

[18] Ozguc, S., Pai, S., Pan, L., Geoghegan, P. J., and Weibel, J. A., "Experimental Demonstration of an Additively Manufactured Vapor Chamber Heat Spreader," *2019 18th IEEE Intersociety Conference on Thermal and Thermomechanical Phenomena in Electronic Systems (ITherm)*, 2019, pp. 416–422. https://doi.org/10.1109/ITHERM.2019.8757359, iSSN: 2577-0799.

[19] Sarraf, D. B., and Anderson, W. G., "Heat Pipes for High Temperature Thermal Management," American Society of Mechanical Engineers Digital Collection, 2010, pp. 707–714. https://doi.org/10.1115/IPACK2007-33984, URL https://asmedigitalcollection.asme.org/InterPACK/proceedings-abstract/InterPACK2007/42770/707/324319.

[20] Lee, H. M., and Kim, D. K., "High-strength AlN ceramics by low-temperature sintering with CaZrO3–Y2O3 co-additives," *Journal of the European Ceramic Society*, Vol. 34, No. 15, 2014, pp. 3627–3633. https://doi.org/10.1016/j.jeurceramsoc.2014.05.008, URL https://www.sciencedirect.com/science/article/pii/S0955221914002660.

[21] Agababov, S. G., "Effect of the roughness factor on radiation properties of solids (experimental check)," *TVT*, Vol. 8, No. 4, 1970, pp. 770–773.

[22] Yu, K., Liu, Y., Liu, D., and Liu, Y., "Normal spectral emissivity characteristics of roughened cobalt and improved emissivity model based on Agababov roughness function," *Applied Thermal Engineering*, Vol. 159, 2019, p. 113957. https://doi.org/10.1016/j.applthermaleng.2019.113957, URL https://www.sciencedirect.com/science/article/pii/S1359431118366912.

[23] Sarraf, D. B., and Anderson, W. G., "Heat Pipes for High Temperature Thermal Management," American Society of Mechanical Engineers Digital Collection, 2010, pp. 707–714. https://doi.org/10.1115/IPACK2007-33984, URL https://asmedigitalcollection.asme.org/InterPACK/proceedings-abstract/InterPACK2007/42770/707/324319.